

A study on multi-frequency electromagnetic imaging

Won-Kwang Park

Department of Mathematics, Kookmin University, Seoul, 136-702, Korea.

Abstract

Recently, a non-iterative multi-frequency imaging algorithm was developed on the basis of an asymptotic expansion formula for thin, curve-like electromagnetic inclusions and the structure of singular vectors in a Multi-Static Response (MSR) matrix. In this paper, we study the structure of a multi-frequency imaging functional and present an improved imaging functional weighted by a given frequency. In order to analyze the function structure, we discover the relationship between the imaging functional and Bessel function of integer order of the first kind. A set of numerical examples for single and multiple inclusions shows that the presented algorithm not only retains the advantages of the traditional function but also improves the imaging performance.

Key words: Multi-frequency imaging, thin electromagnetic inclusion, asymptotic expansion formula, Multi-Static Response (MSR) matrix, Bessel functions, numerical simulations

1. Introduction

In this paper, we consider the problem of inverse scattering from thin curve-like electromagnetic inclusion(s) embedded in a homogeneous domain. Generally, the main purpose of this problem is to identify characteristics of the target of interest, e.g., shape, location, and material properties, but the most important information about a crack or thin electromagnetic inclusion problem considered herein is the shape. Consequently, various shape reconstruction algorithms have been reported in various literature. However, most of these algorithms utilize a Newton-type iteration method, which requires additional of an optimized regularization term, complex evaluation of Fréchet derivatives at each iteration step, and *a priori* information of unknown inclusion(s). However, shape reconstruction via the iteration method with a bad initial guess fails if the above conditions are not completely fulfilled.

For this reason, various non-iterative shape reconstruction algorithms have been developed, such as Multiple Signal Classification (MUSIC) algorithm [5, 17, 20], topological derivative strategy [13, 16], and linear sampling method [7, 12]. Recently, a multi-frequency based algorithm was developed for obtaining a more accurate shape of unknown inclusions. Related articles can be found in [4, 10, 14, 15, 18, 19, 22] and references therein. However, studies have applied this algorithm heuristically and therefore certain phenomena such as appearance of unexpected ghost replicas cannot be explained. This motivated us to explore the structure of multi-frequency imaging algorithm, find optimal conditions for good imaging performance, and improve it to obtain better results.

The analysis of this algorithm is based on the fact that multi-frequency based imaging functional can be represented as a definite integration of the square of the Bessel function of order zero and of the first kind. Using (6) in section 2, we obtain this imaging function at a given frequency ω as follows:

$$\int J_0(\omega x)^2 d\omega = \omega \left(J_0(\omega x)^2 + J_1(\omega x)^2 \right) + \int J_1(\omega x)^2 d\omega,$$

Email address: parkkw@kookmin.ac.kr (Won-Kwang Park)

Preprint submitted to Elsevier

January 27, 2023

where x denotes the location of the unknown target. Hence, one of the way of improvement is to eliminate the last term of the above identity (although it does not significantly contribute to the imaging). For this purpose, we design an alternative imaging functional weighted by applied frequencies.

The rest of this paper is organized as follows. In section 2 we introduce the two-dimensional direct scattering problem and an asymptotic expansion formula for a thin electromagnetic inclusion, and then review the multi-frequency imaging function presented in [4, 14, 15, 18]. In Section 3, we discover and specify the structure and properties of the existing multi-frequency imaging function. We then design an improved imaging function weighted by several applied frequencies and analyze its structure in order to investigate its properties. In section 4, numerical results are discussed in order to verify the effectiveness of the improved imaging function. Finally, section 5 concludes the paper in brief.

Finally, we would like to mention that although the shape constructed using the proposed algorithm does not match the target shape completely, considering it as an initial guess for an iterative algorithm will guarantee a successful reconstruction; for details, refer to [2, 8, 21].

2. Preliminaries

2.1. Direct scattering problem and asymptotic expansion formula

We briefly survey two-dimensional electromagnetic scattering from a thin, curve-like inclusion in a homogeneous domain. For this purpose, let Ω and Υ denote a homogeneous domain with a smooth boundary and a thin inclusion, which is characterized in the neighborhood of a simple, smooth curve γ :

$$\Upsilon = \{\mathbf{x} + \rho\boldsymbol{\eta}(\mathbf{x}) : \mathbf{x} \in \gamma, \rho \in (-h, h)\},$$

where h specifies the thickness of Υ . Throughout this paper, we denote $\boldsymbol{\tau}(x)$ and $\boldsymbol{\eta}(x)$ as the unit tangential and normal, respectively to γ at \mathbf{x} .

Let ε_0 and μ_0 denote the dielectric permittivity and magnetic permeability of Ω , respectively. Similarly, ε and μ denote the permittivity and permeability of Υ , respectively. At a given non-zero frequency ω , let $u^{(l)}(\mathbf{x}; \omega)$ be the time-harmonic total electromagnetic field that satisfies the following boundary value problem:

$$\begin{cases} \nabla \cdot \left(\frac{1}{\mu} \chi(\Upsilon) + \frac{1}{\mu_0} \chi(\Omega \setminus \overline{\Upsilon}) \right) \nabla u^{(l)}(\mathbf{x}; \omega) + \omega^2 \left(\varepsilon \chi(\Upsilon) + \varepsilon_0 \chi(\Omega \setminus \overline{\Upsilon}) \right) u^{(l)}(\mathbf{x}; \omega) = 0 & \text{for } \mathbf{x} \in \Omega \\ \frac{1}{\mu_0} \frac{\partial u^{(l)}(\mathbf{x}; \omega)}{\partial \mathbf{n}(\mathbf{x})} = \frac{1}{\mu_0} \frac{\partial e^{i\omega \boldsymbol{\theta}_l \cdot \mathbf{x}}}{\partial \mathbf{n}(\mathbf{x})} & \text{for } \mathbf{x} \in \partial\Omega \end{cases} \quad (1)$$

with transmission conditions on $\partial\Omega$ and $\partial\Upsilon$. Here, $\{\boldsymbol{\theta}_l : l = 1, 2, \dots, Q\}$ is the set of incident directions equally distributed on the unit circle \mathbb{S}^1 , and χ denotes the characteristic function. Let $u_0^{(l)}(\mathbf{x}; \omega) = e^{i\omega \boldsymbol{\theta}_l \cdot \mathbf{x}}$ be the solution of (1) without Υ . Then, due to the existence of Υ , the following asymptotic expansion formula holds. This formula will contribute to development of the imaging algorithm. A rigorous derivation of this formula can be found in [6].

Theorem 2.1 (Asymptotic expansion formula). *For $\mathbf{x} \in \gamma$ and $\mathbf{y} \in \partial\Omega$, the following asymptotic expansion formula holds:*

$$u^{(l)}(\mathbf{y}; \omega) - u_0^{(l)}(\mathbf{y}; \omega) = h u_{\gamma}^{(l)}(\mathbf{y}; \omega) + o(h),$$

where the perturbation term $u_{\gamma}^{(l)}(\mathbf{x}; \omega)$ is given by

$$u_{\gamma}^{(l)}(\mathbf{y}; \omega) = \int_{\gamma} \left(\omega^2 (\varepsilon - \varepsilon_0) u_0^{(l)}(\mathbf{x}; \omega) \Lambda(\mathbf{x}, \mathbf{y}; \omega) + \nabla u_0^{(l)}(\mathbf{x}; \omega) \cdot \mathbb{M}(\mathbf{x}) \cdot \nabla \Lambda(\mathbf{x}, \mathbf{y}; \omega) \right) d\gamma(\mathbf{x}). \quad (2)$$

Here, $\Lambda(\mathbf{x}, \mathbf{y}; \omega)$ is the Neumann function for Ω that satisfies

$$\begin{cases} \frac{1}{\mu_0} \nabla \cdot \nabla \Lambda(\mathbf{x}, \mathbf{y}; \omega) + \omega^2 \varepsilon_0 \Lambda(\mathbf{x}, \mathbf{y}; \omega) = -\delta(\mathbf{x}, \mathbf{y}) & \text{for } \mathbf{x} \in \Omega \\ \frac{1}{\mu_0} \frac{\partial \Lambda(\mathbf{x}, \mathbf{y}; \omega)}{\partial \mathbf{n}(\mathbf{x})} = 0 & \text{for } \mathbf{x} \in \partial\Omega, \end{cases}$$

and $\mathbb{M}(\mathbf{x})$ is a 2×2 symmetric matrix such that

- $\mathbb{M}(\mathbf{x})$ has eigenvectors $\boldsymbol{\tau}(\mathbf{x})$ and $\boldsymbol{\eta}(\mathbf{x})$,
- eigenvalues corresponding to $\boldsymbol{\tau}(\mathbf{x})$ and $\boldsymbol{\eta}(\mathbf{x})$ are $2\left(\frac{1}{\mu} - \frac{1}{\mu_0}\right)$ and $2\left(\frac{1}{\mu_0} - \frac{\mu}{\mu_0^2}\right)$, respectively.

2.2. Introduction to multi-frequency imaging function

Now, we apply the asymptotic formula (2) in order to introduce the multi-frequency imaging function. Throughout this section, we assume that for a given frequency $\omega = \frac{2\pi}{\lambda}$, γ is divided into M different segments of size of order $\frac{\lambda}{2}$, and only one point, say x_m for $m = 1, 2, \dots, M$, at each segment contributes to the image space of the Multi-Static Response (MSR) matrix $\mathbb{A}(\omega)$ based on the Rayleigh resolution limit; for details, refer to [? 17, 18].

For introducing multi-frequency imaging algorithm, we consider the decomposition of MSR matrix $\mathbb{A}(\omega) = (A_{jl}(\omega)) \in \mathbb{C}^{P \times Q}$, whose element $A_{jl}(\omega)$ is the following normalized boundary measurement:

$$\begin{aligned} A_{jl}(\omega) &= \int_{\partial\Omega} u_\gamma^{(l)}(\mathbf{y}; \omega) \frac{\partial v^{(j)}(\mathbf{y}; \omega)}{\partial \mathbf{n}(\mathbf{y})} dS(\mathbf{y}) = \omega^2 \int_\gamma \left((\varepsilon - \varepsilon_0) + \boldsymbol{\vartheta}_j \cdot \mathbb{M}(\mathbf{x}) \cdot \boldsymbol{\theta}_l \right) e^{-i\omega(\boldsymbol{\vartheta}_j - \boldsymbol{\theta}_l) \cdot \mathbf{x}} d\gamma(\mathbf{x}) \\ &\approx \frac{\omega^2 \text{length}(\gamma)}{M} \sum_{m=1}^M \left[(\varepsilon - \varepsilon_0) + 2\left(\frac{1}{\mu} - \frac{1}{\mu_0}\right) \boldsymbol{\vartheta}_j \cdot \boldsymbol{\tau}(\mathbf{x}_m) \boldsymbol{\theta}_l \cdot \boldsymbol{\tau}(\mathbf{x}_m) \right. \\ &\quad \left. + 2\left(\frac{1}{\mu_0} - \frac{\mu}{\mu_0^2}\right) \boldsymbol{\vartheta}_j \cdot \boldsymbol{\eta}(\mathbf{x}_m) \boldsymbol{\theta}_l \cdot \boldsymbol{\eta}(\mathbf{x}_m) \right] e^{-i\omega(\boldsymbol{\vartheta}_j - \boldsymbol{\theta}_l) \cdot \mathbf{x}_m}, \end{aligned}$$

where $\text{length}(\gamma)$ denotes the length of γ and $v^{(l)}(\mathbf{x}; \omega) = e^{-i\omega \boldsymbol{\vartheta}_j \cdot \mathbf{x}}$, $j = 1, 2, \dots, P$, is a test function. Note that $\{\boldsymbol{\vartheta}_j : j = 1, 2, \dots, P\}$ is the set of unit vectors equally distributed on the unit circle \mathbb{S}^1 .

Based on the above formula, $\mathbb{A}(\omega)$ can be decomposed as follows:

$$\mathbb{A}(\omega) = \mathbb{J}(\omega) \mathbb{D}(\omega) \mathbb{L}(\omega), \quad (3)$$

where $\mathbb{D}(\omega) \in \mathbb{R}^{3M \times 3M}$ is a diagonal matrix with component

$$\frac{\omega^2 \text{length}(\gamma)}{M} \begin{pmatrix} \varepsilon - \varepsilon_0 & 0 \\ 0 & \mathbb{M}(\mathbf{x}_m) \end{pmatrix},$$

and $\mathbb{J}(\omega) \in \mathbb{C}^{P \times 3M}$ and $\mathbb{L}(\omega) \in \mathbb{C}^{3M \times Q}$ are written as

$$\mathbb{J}(\omega) = \left(\mathbf{J}_1(\omega), \mathbf{J}_2(\omega), \dots, \mathbf{J}_M(\omega) \right) \quad \text{and} \quad \mathbb{L}(\omega) = \left(\mathbf{L}_1(\omega), \mathbf{L}_2(\omega), \dots, \mathbf{L}_M(\omega) \right),$$

respectively, where

$$\mathbf{J}_m(\omega) = \begin{pmatrix} e^{i\omega \boldsymbol{\vartheta}_1 \cdot \mathbf{x}_m}, & \boldsymbol{\vartheta}_1 \cdot \boldsymbol{\tau}(\mathbf{x}_m) e^{-i\omega \boldsymbol{\vartheta}_1 \cdot \mathbf{x}}, & \boldsymbol{\vartheta}_1 \cdot \boldsymbol{\eta}(\mathbf{x}_m) e^{-i\omega \boldsymbol{\vartheta}_1 \cdot \mathbf{x}} \\ e^{i\omega \boldsymbol{\vartheta}_2 \cdot \mathbf{x}_m}, & \boldsymbol{\vartheta}_2 \cdot \boldsymbol{\tau}(\mathbf{x}_m) e^{-i\omega \boldsymbol{\vartheta}_2 \cdot \mathbf{x}}, & \boldsymbol{\vartheta}_2 \cdot \boldsymbol{\eta}(\mathbf{x}_m) e^{-i\omega \boldsymbol{\vartheta}_2 \cdot \mathbf{x}} \\ \vdots & \vdots & \vdots \\ e^{i\omega \boldsymbol{\vartheta}_P \cdot \mathbf{x}_m}, & \boldsymbol{\vartheta}_P \cdot \boldsymbol{\tau}(\mathbf{x}_m) e^{-i\omega \boldsymbol{\vartheta}_P \cdot \mathbf{x}}, & \boldsymbol{\vartheta}_P \cdot \boldsymbol{\eta}(\mathbf{x}_m) e^{-i\omega \boldsymbol{\vartheta}_P \cdot \mathbf{x}} \end{pmatrix}$$

and

$$\mathbf{L}_m(\omega) = \begin{pmatrix} e^{i\omega\boldsymbol{\theta}_1 \cdot \mathbf{x}_m}, & \boldsymbol{\theta}_1 \cdot \boldsymbol{\tau}(\mathbf{x}_m)e^{i\omega\boldsymbol{\theta}_1 \cdot \mathbf{x}}, & \boldsymbol{\theta}_1 \cdot \boldsymbol{\eta}(\mathbf{x}_m)e^{i\omega\boldsymbol{\theta}_1 \cdot \mathbf{x}} \\ e^{i\omega\boldsymbol{\theta}_2 \cdot \mathbf{x}_m}, & \boldsymbol{\theta}_2 \cdot \boldsymbol{\tau}(\mathbf{x}_m)e^{i\omega\boldsymbol{\theta}_2 \cdot \mathbf{x}}, & \boldsymbol{\theta}_2 \cdot \boldsymbol{\eta}(\mathbf{x}_m)e^{i\omega\boldsymbol{\theta}_2 \cdot \mathbf{x}} \\ \vdots & \vdots & \vdots \\ e^{i\omega\boldsymbol{\theta}_P \cdot \mathbf{x}_m}, & \boldsymbol{\theta}_Q \cdot \boldsymbol{\tau}(\mathbf{x}_m)e^{i\omega\boldsymbol{\theta}_Q \cdot \mathbf{x}}, & \boldsymbol{\theta}_Q \cdot \boldsymbol{\eta}(\mathbf{x}_m)e^{i\omega\boldsymbol{\theta}_Q \cdot \mathbf{x}} \end{pmatrix}^T.$$

The multi-frequency imaging algorithm developed in [4, 14, 15, 19] is given hereafter; for several frequencies $\{\omega_k : k = 1, 2, \dots, K\}$, Singular Value Decomposition (SVD) of $\mathbb{A}(\omega)$ is performed as follows

$$\mathbb{A}(\omega_k) = \mathbf{U}(\omega_k)\mathbb{S}(\omega_k)\mathbf{V}^*(\omega_k) \approx \sum_{m=1}^{M_k} \sigma_m(\omega_k)\mathbf{U}_m(\omega_k)\mathbf{V}_m^*(\omega_k),$$

where $\sigma_m(\omega_k)$ are nonzero singular values, and $\mathbf{U}_m(\omega_k)$ and $\mathbf{V}_m(\omega_k)$ are respectively the left and right singular vectors of $\mathbb{A}(\omega_k)$. Then, for a *suitable vector* $\boldsymbol{\alpha} \in \mathbb{R}^3 \setminus \{0\}$ and $\mathbf{z} \in \Omega$, define vectors $\mathbf{E}(\mathbf{z}; \omega_k) \in \mathbb{C}^{P \times 1}$ and $\mathbf{F}(\mathbf{z}; \omega) \in \mathbb{C}^{Q \times 1}$ as

$$\begin{aligned} \mathbf{E}(\mathbf{z}; \omega_k) &= \left(\boldsymbol{\alpha} \cdot (1, \boldsymbol{\vartheta}_1)e^{-i\omega\boldsymbol{\vartheta}_1 \cdot \mathbf{z}}, \boldsymbol{\alpha} \cdot (1, \boldsymbol{\vartheta}_2)e^{-i\omega\boldsymbol{\vartheta}_2 \cdot \mathbf{z}}, \dots, \boldsymbol{\alpha} \cdot (1, \boldsymbol{\vartheta}_P)e^{-i\omega\boldsymbol{\vartheta}_P \cdot \mathbf{z}} \right)^T \\ \mathbf{F}(\mathbf{z}; \omega_k) &= \left(\boldsymbol{\alpha} \cdot (1, \boldsymbol{\theta}_1)e^{i\omega\boldsymbol{\theta}_1 \cdot \mathbf{z}}, \boldsymbol{\alpha} \cdot (1, \boldsymbol{\theta}_2)e^{i\omega\boldsymbol{\theta}_2 \cdot \mathbf{z}}, \dots, \boldsymbol{\alpha} \cdot (1, \boldsymbol{\theta}_Q)e^{i\omega\boldsymbol{\theta}_Q \cdot \mathbf{z}} \right)^T, \end{aligned} \quad (4)$$

respectively. Consequently the corresponding unit vector can be generated:

$$\mathbf{W}_J(\mathbf{z}; \omega_k) := \frac{\mathbf{E}(\mathbf{z}; \omega_k)}{|\mathbf{E}(\mathbf{z}; \omega_k)|} \quad \text{and} \quad \mathbf{W}_L(\mathbf{z}; \omega_k) := \frac{\mathbf{F}(\mathbf{z}; \omega_k)}{|\mathbf{F}(\mathbf{z}; \omega_k)|}.$$

Subsequently, we consider the following multi-frequency imaging function (see [4, 14, 15, 18])

$$\mathcal{I}(\mathbf{z}, K) := \left| \sum_{k=1}^K \sum_{m=1}^{M_k} \left(\mathbf{W}_J^*(\mathbf{z}; \omega_k)\mathbf{U}_m(\omega_k) \right) \left(\mathbf{W}_L^*(\mathbf{z}; \omega_k)\bar{\mathbf{V}}_m(\omega_k) \right) \right|,$$

where \bar{a} denotes the complex conjugate of $a \in \mathbb{C}$. Then, by virtue in [4, 14, 15, 18], we get

$$\mathcal{I}(\mathbf{z}, K) \sim \chi(\Upsilon), \quad (5)$$

where $A \sim B$ means that there exists a constant C such that $A = CB$.

Although (5) indicates why the proposed imaging function produces an image of thin inclusion(s), a mathematical analysis is still needed for explaining phenomena such as the appearance of unexpected ghost replicas. In the following section, we analyze the imaging function (5) and improve it for better imaging performance.

3. Introduction to weighted multi-frequency imaging function

3.1. Analysis of multi-frequency imaging function (5)

Now, we analyze the multi-frequency imaging function (5). To do this, we assume that P is sufficiently large and number of nonzero singular values M_k is almost equal to M , for $k = 1, 2, \dots, K$. We then obtain the following results.

Theorem 3.1. Assuming that K is sufficiently large, (5) becomes

$$\mathcal{I}(\mathbf{z}, K) \sim \begin{cases} \sum_{m=1}^M \sum_{q=1}^Q \frac{1}{\sqrt{|\mathbf{z} - \mathbf{x}_m|^2 - (\boldsymbol{\theta}_q \cdot (\mathbf{z} - \mathbf{x}_m))^2}} & , Q \text{ is small and } \omega_K \rightarrow +\infty, \\ \frac{1}{\omega_K - \omega_1} \sum_{m=1}^M \left(\Phi(|\mathbf{z} - \mathbf{x}_m|; \omega_K) - \Phi(|\mathbf{z} - \mathbf{x}_m|; \omega_1) \right) & , Q \text{ is large and } \omega_K < +\infty, \\ \delta(\mathbf{z}, \mathbf{x}_m) & , Q \text{ is large and } \omega_K \rightarrow +\infty. \end{cases}$$

Here, the function $\Phi(t, \omega)$ is given by

$$\Phi(t, \omega) := \omega \left(J_0(\omega t)^2 + J_1(\omega t)^2 \right) + \int_0^\omega J_1(xt)^2 dx,$$

where $J_\nu(t)$ denotes the Bessel function of order ν and of the first kind and δ denotes the Dirac delta function.

Proof. First, assume that Q is sufficiently large and that $\omega_K < +\infty$. We denote $\Delta \boldsymbol{\vartheta}_p := |\boldsymbol{\vartheta}_p - \boldsymbol{\vartheta}_{p-1}|$ for $p = 2, 3, \dots, P$, and $\boldsymbol{\vartheta}_1 := |\boldsymbol{\vartheta}_1 - \boldsymbol{\vartheta}_N|$. Notation $\Delta \boldsymbol{\theta}_q$ can be defined analogously.

Since the following property (see [4]) holds

$$\mathbf{W}_J(\mathbf{z}; \omega_k) \simeq \mathbf{U}_m(\omega_k) \quad \text{and} \quad \mathbf{W}_L(\mathbf{z}; \omega_k) \simeq \overline{\mathbf{V}_m}(\omega_k),$$

plugging the above relationship into (5) and applying [10, Lemma 4.1], we observe that

$$\begin{aligned} \mathcal{I}(\mathbf{z}, K) &\sim \left| \sum_{k=1}^K \sum_{m=1}^M \left(\mathbf{W}_J^*(\mathbf{z}; \omega_k) \mathbf{W}_J(\mathbf{x}_m; \omega_k) \right) \left(\mathbf{W}_L^*(\mathbf{z}; \omega_k) \mathbf{W}_L(\mathbf{x}_m; \omega_k) \right) \right| \\ &\approx \left| \sum_{k=1}^K \sum_{m=1}^M \left(\sum_{p=1}^P e^{i\omega_k \boldsymbol{\vartheta}_p \cdot (\mathbf{z} - \mathbf{x}_m)} \right) \left(\sum_{q=1}^Q e^{i\omega_k \boldsymbol{\theta}_q \cdot (\mathbf{z} - \mathbf{x}_m)} \right) \right| \\ &\approx \left| \sum_{k=1}^K \sum_{m=1}^M \left(\frac{1}{2\pi} \sum_{p=1}^P e^{i\omega_k \boldsymbol{\vartheta}_p \cdot (\mathbf{z} - \mathbf{x}_m)} \Delta \boldsymbol{\vartheta}_p \right) \left(\frac{1}{2\pi} \sum_{q=1}^Q e^{i\omega_k \boldsymbol{\theta}_q \cdot (\mathbf{z} - \mathbf{x}_m)} \Delta \boldsymbol{\theta}_q \right) \right| \\ &\approx \frac{1}{4\pi^2} \left| \sum_{k=1}^K \sum_{m=1}^M \left(\int_{\mathbb{S}^1} e^{i\omega_k \boldsymbol{\theta} \cdot (\mathbf{z} - \mathbf{x}_m)} d\boldsymbol{\theta} \right)^2 \right| \approx \frac{1}{\omega_K - \omega_1} \left| \sum_{m=1}^M \int_{\omega_1}^{\omega_K} J_0(\omega |\mathbf{z} - \mathbf{x}_m|)^2 d\omega \right|. \end{aligned} \tag{6}$$

Then, applying the indefinite integral (see [23, Page 35]¹)

$$\int J_0(t)^2 dt = t \left(J_0(t)^2 + J_1(t)^2 \right) + \int J_1(t)^2 dt$$

with a change of variable $\omega |\mathbf{z} - \mathbf{x}_m| = t$ yields

$$\begin{aligned} \mathcal{I}(\mathbf{z}, K) &\sim \left| \sum_{m=1}^M \frac{1}{|\mathbf{z} - \mathbf{x}_m|} \int_{\omega_1 |\mathbf{z} - \mathbf{x}_m|}^{\omega_K |\mathbf{z} - \mathbf{x}_m|} J_0(t)^2 dt \right| \\ &= \left| \sum_{m=1}^M \left[\frac{\omega_K}{\omega_K - \omega_1} \left(J_0(\omega_K |\mathbf{z} - \mathbf{x}_m|)^2 + J_1(\omega_K |\mathbf{z} - \mathbf{x}_m|)^2 \right) + \int_0^{\omega_K} J_1(\omega |\mathbf{z} - \mathbf{x}_m|)^2 d\omega \right] \right. \\ &\quad \left. - \frac{\omega_1}{\omega_K - \omega_1} \left(J_0(\omega_1 |\mathbf{z} - \mathbf{x}_m|)^2 + J_1(\omega_1 |\mathbf{z} - \mathbf{x}_m|)^2 \right) + \int_0^{\omega_1} J_1(\omega |\mathbf{z} - \mathbf{x}_m|)^2 d\omega \right| \\ &= \frac{1}{\omega_K - \omega_1} \left| \sum_{m=1}^M \left(\Phi(|\mathbf{z} - \mathbf{x}_m|; \omega_K) - \Phi(|\mathbf{z} - \mathbf{x}_m|; \omega_1) \right) \right|. \end{aligned}$$

¹In our knowledge, there is no finite representation of the integral $\int J_\nu(t)^2 dt$ for an integer ν .

Consequently, if we assume $\omega_K \rightarrow +\infty$, then

$$\mathcal{I}(\mathbf{z}, K) \sim \delta(\mathbf{z}, \mathbf{x}_m).$$

Next, we assume that Q is small and that $\omega_K \rightarrow +\infty$. Then

$$\begin{aligned} \mathcal{I}(\mathbf{z}, K) &\approx \left| \sum_{k=1}^K \sum_{m=1}^M \left(\sum_{p=1}^P e^{i\omega_k \boldsymbol{\vartheta}_p \cdot (\mathbf{z} - \mathbf{x}_m)} \right) \left(\sum_{q=1}^Q e^{i\omega_k \boldsymbol{\theta}_q \cdot (\mathbf{z} - \mathbf{x}_m)} \right) \right| \\ &\sim \left| \sum_{m=1}^M \sum_{q=1}^Q \int_{\omega_1}^{\omega_K} e^{i\omega \boldsymbol{\theta}_q \cdot (\mathbf{z} - \mathbf{x}_m)} J_0(\omega |\mathbf{z} - \mathbf{x}_m|) d\omega \right|. \end{aligned}$$

Since $\boldsymbol{\theta}_q \in \mathbb{S}^1$, we note that

$$|\mathbf{z} - \mathbf{x}_m|^2 - (\boldsymbol{\theta}_q \cdot (\mathbf{z} - \mathbf{x}_m))^2 = |\mathbf{z} - \mathbf{x}_m|^2 \left[1 - \left(\boldsymbol{\theta}_q \cdot \frac{\mathbf{z} - \mathbf{x}_m}{|\mathbf{z} - \mathbf{x}_m|} \right)^2 \right] \geq 0.$$

Hence, applying the identity (see [9, formula 6.671, page 717])

$$\int_0^\infty e^{iat} J_\nu(bt) dt = \frac{1}{\sqrt{b^2 - a^2}} \left[\cos\left(\nu \sin^{-1} \frac{a}{b}\right) + i \sin\left(\nu \sin^{-1} \frac{a}{b}\right) \right] \quad \text{for } a < b$$

yields

$$\lim_{\omega_K \rightarrow +\infty} \int_{\omega_1}^{\omega_K} e^{i\omega \boldsymbol{\theta}_q \cdot (\mathbf{z} - \mathbf{x}_m)} J_0(\omega |\mathbf{z} - \mathbf{x}_m|)^2 d\omega \approx \frac{1}{\sqrt{|\mathbf{z} - \mathbf{x}_m|^2 - (\boldsymbol{\theta}_q \cdot (\mathbf{z} - \mathbf{x}_m))^2}}.$$

□

Remark 3.2. Theorem 3.1 indicates certain properties of (5), which are summarized as follows:

1. $J_0(x)$ has an oscillation property. Hence, if a small value of K is considered, the identification of shape of Υ will be interrupted by ghost replicas.
2. On the other hand, if a large number of frequencies are applied, $\mathcal{I}(\mathbf{z}, K)$ will exhibit an accurate shape of Υ . Note that this fact can be validated via Statistical Hypothesis Testing (refer to [4] for more details).
3. When Q is small, $\mathcal{I}(\mathbf{z}, K)$ plots a large magnitude at \mathbf{z} satisfying

$$\mathbf{z} = \mathbf{x}_m \in \Upsilon \quad \text{and} \quad \boldsymbol{\theta}_q = \pm \frac{\mathbf{z} - \mathbf{x}_m}{|\mathbf{z} - \mathbf{x}_m|}.$$

This means that $\mathcal{I}(\mathbf{z}, K)$ produces not only the shape of Υ but also unexpected ghost replicas.

4. When low frequencies ω_k are applied such that $\omega_k |\mathbf{z} - \mathbf{x}_m| \approx 0$, $\mathcal{I}(\mathbf{z}, K)$ will fail to produce the shape of Υ . However, if sufficiently high frequencies ω_k are applied, the term

$$\Theta(|\mathbf{z} - \mathbf{x}_m|, \omega) := \int_{\omega_1}^{\omega_K} J_1(\omega |\mathbf{z} - \mathbf{x}_m|)^2 d\omega \ll O(\omega_K)$$

becomes negligible (see [11]) and hence the shape of Υ can be easily constructed by $\mathcal{I}(\mathbf{z}, K)$. This is the reason why applying high frequency yields good results.

5. For a small value of K , if $\omega_K \rightarrow +\infty$ then it is expected that $\mathcal{I}(\mathbf{z}, K)$ will yields a good result. however, this is an ideal assumption.

3.2. Permeability contrast case: why do two ghost replicas appear in the numerical experiments?

In section 2, although we did not focused on the vector α , it is important. In order to determine the influence of α on imaging performance, let us define vectors $\mathbf{E}(\mathbf{z}; \omega_k) \in \mathbb{C}^{P \times 1}$ and $\mathbf{F}(\mathbf{z}; \omega) \in \mathbb{C}^{Q \times 1}$ in (4) as

$$\mathbf{E}(\mathbf{z}; \omega_k) = \left(e^{-i\omega \boldsymbol{\vartheta}_1 \cdot \mathbf{z}}, e^{-i\omega \boldsymbol{\vartheta}_2 \cdot \mathbf{z}}, \dots, e^{-i\omega \boldsymbol{\vartheta}_P \cdot \mathbf{z}} \right)^T, \quad \mathbf{F}(\mathbf{z}; \omega_k) = \left(e^{i\omega \boldsymbol{\theta}_1 \cdot \mathbf{z}}, e^{i\omega \boldsymbol{\theta}_2 \cdot \mathbf{z}}, \dots, e^{i\omega \boldsymbol{\theta}_Q \cdot \mathbf{z}} \right)^T, \quad (7)$$

and corresponding unit vectors $\mathbf{W}_J(\mathbf{z}; \omega_k)$ and $\mathbf{W}_L(\mathbf{z}; \omega_k)$. Then applying [10, Lemma 4.1], $\mathcal{I}(\mathbf{z}, K)$ becomes

$$\begin{aligned} \mathcal{I}(\mathbf{z}, K) &\sim \left| \sum_{k=1}^K \sum_{m=1}^M \left(\mathbf{W}_J^*(\mathbf{z}; \omega_k) \mathbf{U}_m(\omega_k) \right) \left(\mathbf{W}_L^*(\mathbf{z}; \omega_k) \mathbf{V}_m(\omega_k) \right) \right| \\ &\approx \left| \sum_{k=1}^K \sum_{m=1}^M \left(\sum_{p=1}^P \boldsymbol{\vartheta}_p \cdot (\boldsymbol{\tau}(\mathbf{x}_m) + \boldsymbol{\eta}(\mathbf{x}_m)) e^{i\omega_k \boldsymbol{\vartheta}_p \cdot (\mathbf{z} - \mathbf{x}_m)} \right) \left(\sum_{q=1}^Q \boldsymbol{\theta}_q \cdot (\boldsymbol{\tau}(\mathbf{x}_m) + \boldsymbol{\eta}(\mathbf{x}_m)) e^{i\omega_k \boldsymbol{\theta}_q \cdot (\mathbf{z} - \mathbf{x}_m)} \right) \right| \\ &\approx \left| \sum_{k=1}^K \sum_{m=1}^M \left(\int_{\mathbb{S}^1} \boldsymbol{\theta} \cdot (\boldsymbol{\tau}(\mathbf{x}_m) + \boldsymbol{\eta}(\mathbf{x}_m)) e^{i\omega_k \boldsymbol{\theta} \cdot (\mathbf{z} - \mathbf{x}_m)} d\boldsymbol{\theta} \right)^2 \right| \\ &\sim \left| \sum_{m=1}^M \int_{\omega_1}^{\omega_K} \left((\mathbf{z} - \mathbf{x}_m) \cdot (\boldsymbol{\tau}(\mathbf{x}_m) + \boldsymbol{\eta}(\mathbf{x}_m)) J_1(\omega |\mathbf{z} - \mathbf{x}_m|) \right)^2 d\omega \right| \sim \sum_{m=1}^M \int_{\omega_1}^{\omega_K} J_1(\omega |\mathbf{z} - \mathbf{x}_m|)^2 d\omega. \end{aligned}$$

Note that $J_1(\omega x)$ is maximum at two points x_1 and x_2 , and is symmetric with respect to x (see Figure 1). This means that $\mathcal{I}(\mathbf{z}, K)$ plots 0 on Υ and two ghost replicas in the neighborhood of Υ (see Figure 2). This means α must be a linear combination of $\boldsymbol{\tau}(\mathbf{x}_m)$ and $\boldsymbol{\eta}(\mathbf{x}_m)$. Unfortunately, we have no *prior* information of Υ . Hence, finding an optimal α is an interesting research topic.

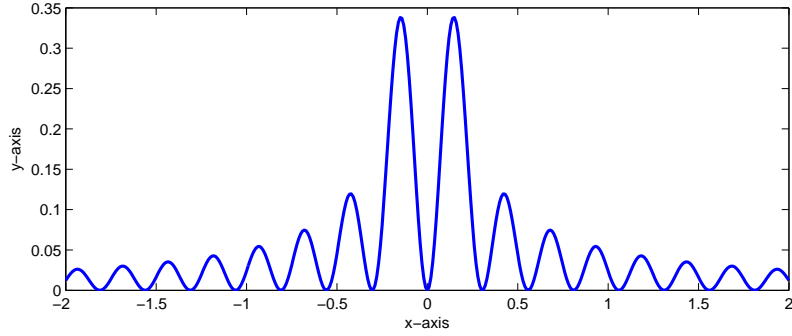


Figure 1: Graph of $y = J_1(\omega|x|)^2$ for $\omega = 2\pi/0.5$.

3.3. Weighted multi-frequency imaging function: Introduction and analysis

Remark 3.2 shows the optimal conditions (P and Q are sufficiently large and $\omega_K \rightarrow +\infty$) for imaging. However, real-world applications, a high frequency such as $+\infty$ cannot be applied. Therefore, in order to improve (5), we propose a multi-frequency imaging function weighted by $(\omega_k)^n$ as follows:

$$\mathcal{I}(\mathbf{z}, K; n) = \left| \sum_{k=1}^K \sum_{m=1}^{M_k} (\omega_k)^n \left(\mathbf{W}_J^*(\mathbf{z}; \omega_k) \mathbf{U}_m(\omega_k) \right) \left(\mathbf{W}_L^*(\mathbf{z}; \omega_k) \overline{\mathbf{V}_m(\omega_k)} \right) \right|. \quad (8)$$

Note that $\mathcal{I}(\mathbf{z}, K; 0) = \mathcal{I}(\mathbf{z}, K)$. Consequently, the following question arises:

Does a large value of order n contributes significantly to the imaging performance?

The answer is *no*. To find out how, the structure of (8) is explored as follows.

Theorem 3.3. *Let K and ω_K have sufficiently large values and $\omega_K < +\infty$. Then for a natural number n , (8) satisfies*

$$\mathcal{I}(\mathbf{z}, K; n) \sim \sum_{m=1}^M \left(\hat{\Phi}(|\mathbf{z} - \mathbf{x}_m|, \omega_K; n) - \hat{\Phi}(|\mathbf{z} - \mathbf{x}_m|, \omega_1; n) \right), \quad (9)$$

where $\hat{\Phi}$ is given by

$$\hat{\Phi}(t, \omega; n) := \omega^{n+1} \left(J_0(\omega t)^2 + J_1(\omega t)^2 \right).$$

Proof. First, let us assume that n is an odd number, say $n = 2s + 1$. In order to examine the structure of (8), we recall a recurrence formula (see [23, page 14])

$$\int t^{2n+1} J_0(t)^2 dt = \frac{1}{2n+1} \left[\frac{t^{2n+2}}{2} \left(J_0(t)^2 + J_1(t)^2 \right) + n^2 t^{2n} J_0(t)^2 + n t^{2n+1} J_0(t) J_1(t) - 2n^3 \int t^{2n-1} J_0(t)^2 dt \right]. \quad (10)$$

Then, applying (10) with a change of variable $\omega|\mathbf{z} - \mathbf{x}_m| = t$ in (8) induces

$$\begin{aligned} \mathcal{I}(\mathbf{z}, K; 2s+1) &\sim \left| \sum_{m=1}^M \frac{1}{|\mathbf{z} - \mathbf{x}_m|^{2s+2}} \int_{\omega_1|\mathbf{z} - \mathbf{x}_m|}^{\omega_K|\mathbf{z} - \mathbf{x}_m|} t^{2s+1} J_0(t)^2 dt \right| \\ &= \left| \sum_{m=1}^M \left(\Psi_1(|\mathbf{z} - \mathbf{x}_m|, \omega_K, \omega_1; s) + \Psi_2(|\mathbf{z} - \mathbf{x}_m|, \omega_K, \omega_1; s) \right. \right. \\ &\quad \left. \left. + \Psi_3(|\mathbf{z} - \mathbf{x}_m|, \omega_K, \omega_1; s) - \Psi_4(|\mathbf{z} - \mathbf{x}_m|, \omega_K, \omega_1; s) \right) \right|, \end{aligned}$$

where

$$\begin{aligned} \Psi_1(t, \omega_K, \omega_1; s) &:= \frac{(\omega_K)^{2s+2}}{4s+2} \left(J_0(\omega_K t)^2 + J_1(\omega_K t)^2 \right) - \frac{(\omega_1)^{2s+2}}{4s+2} \left(J_0(\omega_1 t)^2 + J_1(\omega_1 t)^2 \right), \\ \Psi_2(t, \omega_K, \omega_1; s) &:= \frac{s^2}{(2s+1)t^2} \left((\omega_K)^{2s} J_0(\omega_K t)^2 - (\omega_1)^{2s} J_0(\omega_1 t)^2 \right), \\ \Psi_3(t, \omega_K, \omega_1; s) &:= \frac{s(\omega_K)^{2s+1}}{(2s+1)t} J_0(\omega_K t) J_1(\omega_K t) - \frac{s(\omega_1)^{2s+1}}{(2s+1)t} J_0(\omega_1 t) J_1(\omega_1 t), \end{aligned} \quad (11)$$

and

$$\Psi_4(|\mathbf{z} - \mathbf{x}_m|, \omega_K, \omega_1; s) := \frac{2s^3}{(2s+1)|\mathbf{z} - \mathbf{x}_m|^2} \mathcal{I}(\mathbf{z}, K; 2s-1).$$

Now, we assume that ω_k is sufficiently large, \mathbf{z} satisfies $\mathbf{z} \neq \mathbf{x}_m$ and $|\mathbf{z} - \mathbf{x}_m| \gg \frac{3}{4\omega_K}$. Then, applying the asymptotic form of the Bessel function

$$J_\nu(t) \approx \sqrt{\frac{2}{\pi t}} \cos \left(t - \frac{\nu\pi}{2} - \frac{\pi}{4} \right) \quad (12)$$

yields

$$\frac{J_0(\omega_K|\mathbf{z} - \mathbf{x}_m|)^2}{|\mathbf{z} - \mathbf{x}_m|^2} \approx \frac{2}{\omega_K|\mathbf{z} - \mathbf{x}_m|^{3\pi}} \cos \left(\omega_K|\mathbf{z} - \mathbf{x}_m| - \frac{\pi}{4} \right) \ll \frac{128(\omega_K)^2}{27\pi} \cos \left(\omega_K|\mathbf{z} - \mathbf{x}_m| - \frac{\pi}{4} \right),$$

and

$$\begin{aligned} \frac{J_0(\omega_K|\mathbf{z} - \mathbf{x}_m|)J_1(\omega_K|\mathbf{z} - \mathbf{x}_m|)}{|\mathbf{z} - \mathbf{x}_m|} &\approx \frac{2}{\omega_K|\mathbf{z} - \mathbf{x}_m|^{2\pi}} \cos\left(\omega_K|\mathbf{z} - \mathbf{x}_m| - \frac{\pi}{4}\right) \cos\left(\omega_K|\mathbf{z} - \mathbf{x}_m| - \frac{3\pi}{4}\right) \\ &\ll \frac{32\omega_K}{9\pi} \cos\left(\omega_K|\mathbf{z} - \mathbf{x}_m| - \frac{\pi}{4}\right) \cos\left(\omega_K|\mathbf{z} - \mathbf{x}_m| - \frac{3\pi}{4}\right). \end{aligned}$$

Hence, we can observe that

$$\begin{aligned} \Psi_2(|\mathbf{z} - \mathbf{x}_m|, \omega_K, \omega_1; s) &\ll O((\omega_k)^{2s+2}) = \Psi_1(|\mathbf{z} - \mathbf{x}_m|, \omega_K, \omega_1; s), \\ \Psi_3(|\mathbf{z} - \mathbf{x}_m|, \omega_K, \omega_1; s) &\ll O((\omega_k)^{2s+2}) = \Psi_1(|\mathbf{z} - \mathbf{x}_m|, \omega_K, \omega_1; s), \\ \Psi_4(|\mathbf{z} - \mathbf{x}_m|, \omega_K, \omega_1; s) &\ll \frac{32s^3(\omega_K)^2}{9(2s+1)} \mathcal{I}(\mathbf{z}, K; 2s-1) = O((\omega_k)^{2s+1}). \end{aligned}$$

This means that the terms Ψ_2 , Ψ_3 , and Ψ_4 are dominated by Ψ_1 . Hence, we conclude that for an odd number n , (9) holds.

Next, let us assume that n is an even number, say $n = 2s$. Similar to the case of an odd number n , we recall a recurrence formula (see [23, page 35])

$$\int t^{2n} J_0(t)^2 dt = A_n(t)J_0(t)^2 + B_n(t)J_0(t)J_1(t) + C_n(t)J_1(t)^2 + D_n \int J_0(t)^2 dt, \quad (13)$$

where

$$A_n(t) = \sum_{r=1}^{n+1} a_r t^{2r-1}, \quad B_n(t) = \sum_{r=1}^n b_r t^{2r}, \quad C_n(t) = \sum_{r=1}^n c_r t^{2r+1},$$

and a_r, b_r, c_r , and D_n are constants. Then, applying a change of variable $t = \omega|\mathbf{z} - \mathbf{x}_m|$ in (13) yields

$$\begin{aligned} \mathcal{I}(\mathbf{z}, K; 2s) &\sim \left| \sum_{m=1}^M \frac{1}{|\mathbf{z} - \mathbf{x}_m|^{2s+1}} \int_{\omega_1|\mathbf{z} - \mathbf{x}_m|}^{\omega_K|\mathbf{z} - \mathbf{x}_m|} t^{2s} J_0(t)^2 dt \right| \\ &= \left| \sum_{m=1}^M \left(\Psi_5(|\mathbf{z} - \mathbf{x}_m|, \omega_K, \omega_1; s) + \Psi_6(|\mathbf{z} - \mathbf{x}_m|, \omega_K, \omega_1; s) \right. \right. \\ &\quad \left. \left. + \Psi_7(|\mathbf{z} - \mathbf{x}_m|, \omega_K, \omega_1; s) - \Psi_8(|\mathbf{z} - \mathbf{x}_m|, \omega_K, \omega_1; s) \right) \right|, \end{aligned}$$

where

$$\begin{aligned} \Psi_5(t, \omega_K, \omega_1; s) &:= \frac{1}{t^{2s+1}} \sum_{r=1}^{s+1} \left(a_r (\omega_K t)^{2r-1} J_0(\omega_K t)^2 - a_r (\omega_1 t)^{2r-1} J_0(\omega_1 t)^2 \right), \\ \Psi_6(t, \omega_K, \omega_1; s) &:= \frac{1}{t^{2s+1}} \sum_{r=1}^s \left(b_r (\omega_K t)^{2r} J_0(\omega_K t) J_1(\omega_K t) - b_r (\omega_1 t)^{2r} J_0(\omega_1 t) J_1(\omega_1 t) \right), \\ \Psi_7(t, \omega_K, \omega_1; s) &:= \frac{1}{t^{2s+1}} \sum_{r=1}^s \left(c_r (\omega_K t)^{2r+1} J_1(\omega_K t)^2 - c_r (\omega_1 t)^{2r+1} J_1(\omega_1 t)^2 \right), \end{aligned}$$

and

$$\Psi_8(|\mathbf{z} - \mathbf{x}_m|, \omega_K, \omega_1; s) = \frac{D_n}{|\mathbf{z} - \mathbf{x}_m|^{2s}} \mathcal{I}(\mathbf{z}, K).$$

Now, we assume that ω_k is sufficiently large, \mathbf{z} satisfies $\mathbf{z} \neq \mathbf{x}_m$, and $|\mathbf{z} - \mathbf{x}_m| \gg \frac{3}{4\omega_K}$. Then applying (12) yields

$$\sum_{r=1}^s a_r (\omega_K |\mathbf{z} - \mathbf{x}_m|)^{2r-1} \ll \sum_{r=1}^s a_r \left(\frac{4}{3} \right)^{2r-1} \leq \max_{1 \leq r \leq s} \{a_r\} \frac{12 \cdot (4^{2s} - 3^{2s})}{7 \cdot 3^{2s}}.$$

Accordingly, we obtain

$$\begin{aligned}\Psi_5(|\mathbf{z} - \mathbf{x}_m|, \omega_K, \omega_1; s) &\sim \left((\omega_K)^{2s+1} J_0(\omega_K |\mathbf{z} - \mathbf{x}_m|)^2 - (\omega_1)^{2s+1} J_0(\omega_1 |\mathbf{z} - \mathbf{x}_m|)^2 \right), \\ \Psi_6(|\mathbf{z} - \mathbf{x}_m|, \omega_K, \omega_1; s) &\ll \Psi_5(|\mathbf{z} - \mathbf{x}_m|, \omega_K, \omega_1; s), \\ \Psi_7(|\mathbf{z} - \mathbf{x}_m|, \omega_K, \omega_1; s) &\sim \left((\omega_K)^{2s+1} J_1(\omega_K |\mathbf{z} - \mathbf{x}_m|)^2 - (\omega_1)^{2s+1} J_1(\omega_1 |\mathbf{z} - \mathbf{x}_m|)^2 \right), \\ \Psi_8(|\mathbf{z} - \mathbf{x}_m|, \omega_K, \omega_1; s) &\ll \left(\frac{4\omega_K}{3} \right)^{2s} D_n \mathcal{I}(\mathbf{z}, K) = O((\omega_k)^{2s+1}).\end{aligned}$$

Hence, we conclude that for an even number n , (9) holds. \square

Remark 3.4. Based on Theorem 3.3, we can determine following properties of (8), as summarized below:

- (P1). Increasing n in (8) does not influence the imaging performance. In fact, $\mathbf{n} = \mathbf{1}$ is the best choice for obtaining good results because the terms $\Psi_l(|\mathbf{z} - \mathbf{x}_m|, \omega_K, \omega_1; s)$, $l = 2, 3, \dots, 8$, in (8) are eliminated.
- (P2). Similar to (5), applying low frequencies ω_k such that $\omega_k |\mathbf{z} - \mathbf{x}_m| \approx 0$ degrades the results. Hence, sufficiently high frequencies must be applied.
- (P3). When n is an odd number, $\mathcal{I}(\mathbf{z}, K; n)$ does not contain

$$\int_{\omega_1}^{\omega_K} J_1(\omega |\mathbf{z} - \mathbf{x}_m|)^2 d\omega$$

but it is a part of $\mathcal{I}(\mathbf{z}, K; n)$ when n is an even number. This means that, although $\mathcal{I}(\mathbf{z}, K; n)$ offers good results, large numbers of unexpected replicas will appear in the map of $\mathcal{I}(\mathbf{z}, K; n)$ when n is even and ω_K is large. Hence, for an integer s , $\mathcal{I}(\mathbf{z}, K; 2s - 1)$ offers better results than $\mathcal{I}(\mathbf{z}, K; 2s)$.

4. Numerical experiments

In this section, a set of numerical experiments are performed. Throughout this section, the homogeneous domain Ω is selected as a unit circle and two γ_j are chosen to describe thin inclusions Υ_j as

$$\begin{aligned}\gamma_1 &= \{(z - 0.2, -0.5z^2 + 0.4) : z \in [-0.5, 0.5]\} \\ \gamma_2 &= \{(z + 0.2, z^3 + z^2 - 0.5) : z \in [-0.5, 0.5]\}.\end{aligned}$$

The thickness of all the thin inclusion(s) is set to $h = 0.015$, and $\varepsilon_0 = \mu_0 = 1$ and $\varepsilon_j = \mu_j = 5$. For given wavelengths λ_k , the applied frequencies are $\omega_k = \frac{2\pi}{\lambda_k}$, which are varied between $\omega_1 = \frac{2\pi}{0.7}$ and $\omega_K = \frac{2\pi}{0.3}$. In every example, $K = 10$ different frequencies are applied.

A set of vectors $\{\boldsymbol{\vartheta}_j : j = 1, 2, \dots, P\}$ and $\{\boldsymbol{\theta}_l : l = 1, 2, \dots, Q\}$ on \mathbb{S}^1 are selected as

$$\boldsymbol{\vartheta}_j = \left(\cos \frac{2\pi j}{P}, \sin \frac{2\pi j}{P} \right) \quad \text{and} \quad \boldsymbol{\theta}_l = - \left(\cos \frac{2\pi l}{Q}, \sin \frac{2\pi l}{Q} \right),$$

respectively. In our examples, we set, $P = 24$ and $Q = 20$. Vector $\boldsymbol{\alpha}$ in (4) is set to $\boldsymbol{\alpha} = (1, 0, 0)$.

For every example, white Gaussian noise with a Signal-to-Noise Ratio (SNR) of 10dB is added to the unperturbed boundary measurement data using the MATLAB command `awgn` in order to demonstrate the effectiveness of the proposed algorithm. For discriminating non-zero singular values, a 0.01-threshold strategy is adopted (see [19] for instance).

First, let us consider the imaging of Υ_1 when only magnetic permeability contrast exists, at a fixed frequency $\omega = \frac{2\pi}{0.5}$. From the result in section 3.2, it is clear that two ghost replicas appear in the neighborhood of Υ_1 when we select vectors $\mathbf{E}(\mathbf{z}; \omega_k)$ and $\mathbf{F}(\mathbf{z}; \omega)$ in (7). Note that based on the shape of Υ_1 , $\tau(\mathbf{x}_m) \approx 0$ and $\boldsymbol{\eta}(\mathbf{x}_m) \approx 1$. Hence setting of $\boldsymbol{\alpha} = (0, 1)$ yields a good result while $\boldsymbol{\alpha} = (1, 0)$ offers a poor result, as shown in Figure 2.

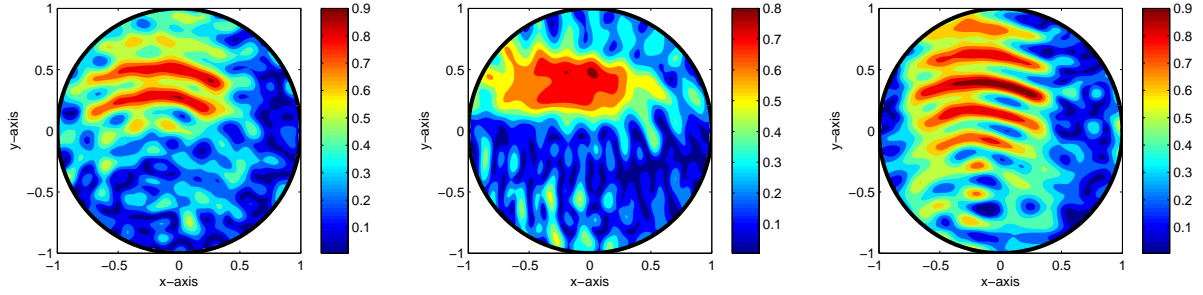


Figure 2: [Permeability contrast case only] Maps of $\mathcal{I}(\mathbf{z}, 0)$ with vectors in (7) (left), $\alpha = (1, 0)$ (center), and $\alpha = (0, 1)$ (right) when the thin inclusion is Υ_1 .

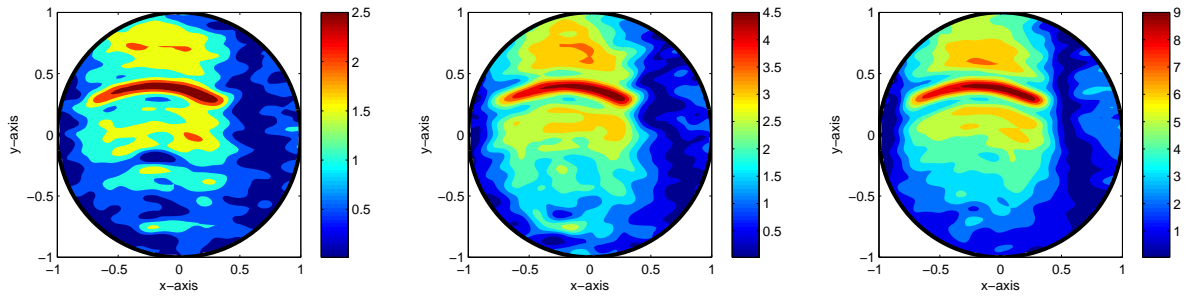


Figure 3: [Permeability contrast case only] Maps of $\mathcal{I}(\mathbf{z}, n)$ with $\alpha = (0, 1)$ for $n = 3$ (left), $n = 5$ (center), and $n = 10$ (right) when the thin inclusion is Υ_1 .

Figure 3 shows the effect of the number of frequencies on the imaging performance. By comparing the results with those in Figure 2, we observe that applying multiple frequencies guarantees better results than applying a single frequency does.

Hereafter, we consider the imaging of thin inclusions when both permittivity and permeability contrast exist. Figure 4 shows the maps of $\mathcal{I}(\mathbf{z}, 10; n)$ for $n = 0, 1$, and 2 . The overall results show that although $\mathcal{I}(\mathbf{z}, 10; n)$ offers good imaging performance, odd number of n yields better results than an even number of n does, refer to (P3) of Remark 3.4.

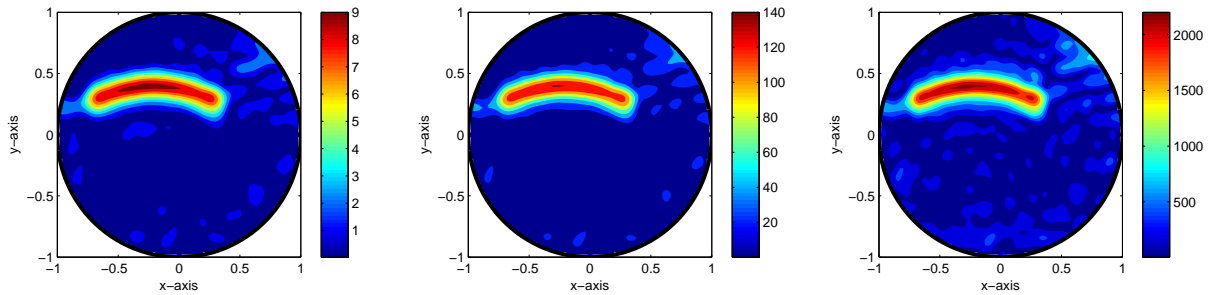


Figure 4: Maps of $\mathcal{I}(\mathbf{z}, 10; n)$ for $n = 0$ (left), $n = 1$ (center), and $n = 2$ (right) when the thin inclusion is Υ_1 .

Now, we consider the maps of $\mathcal{I}(\mathbf{z}, 10; n)$ for $n = 5, 6$, and 7 . The corresponding results illustrated in Figure 5 indicate that increasing n not only contributes negligibly to the imaging performance but also

generates large numbers of unexpected replicas. This result supports (P1) of Remark 3.4.

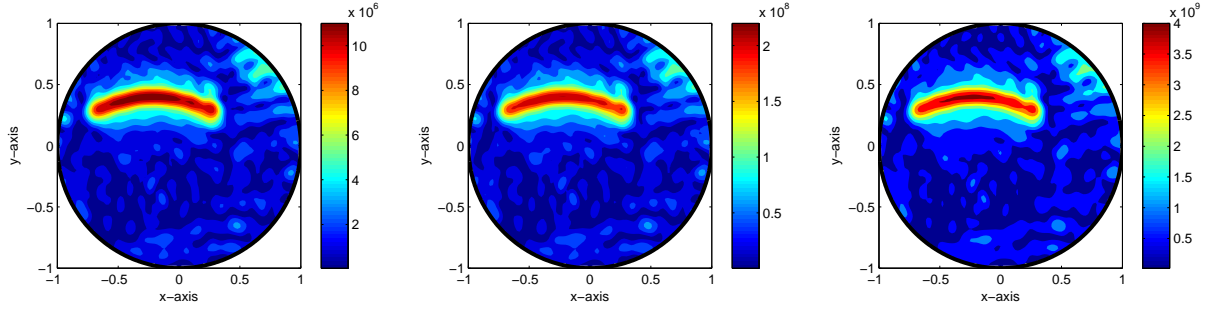


Figure 5: Maps of $\mathcal{I}(\mathbf{z}, 10; n)$ for $n = 5$ (left), $n = 6$ (center), and $n = 7$ (right) when the thin inclusion is Υ_1 .

Figure 6 shows the maps of $\mathcal{I}(\mathbf{z}, 10; n)$ for $n = 0, 1$, and 2 when the thin inclusion is Υ_2 . Similar to Figure 4, the map of $\mathcal{I}(\mathbf{z}, 10; 1)$ demonstrates very good imaging performance but the resolution is poor at $\mathbf{z} = (0.6 \ -0.24)$ on the large curvature.

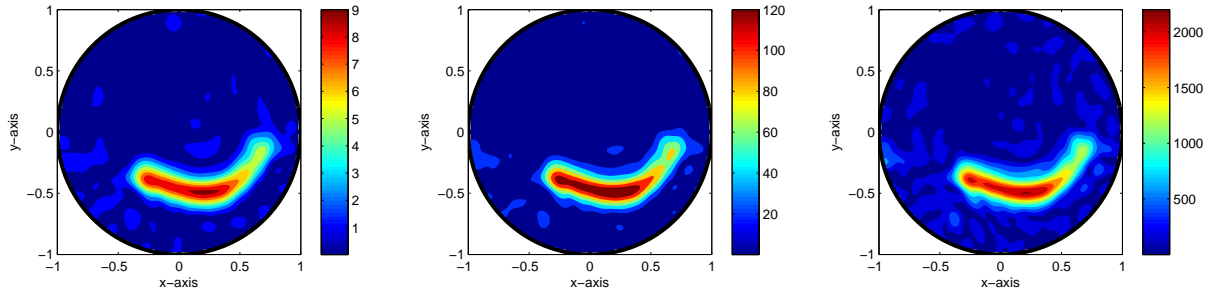


Figure 6: Same as Figure 4 except that the thin inclusion is Υ_2 .

For the final example, we consider imaging of multiple inclusions $\Upsilon_1 \cup \Upsilon_2$ with $\varepsilon_1 = \mu_1 = 5$ and $\varepsilon_2 = \mu_2 = 10$. Figure 7 shows the maps of $\mathcal{I}(\mathbf{z}, 10; n)$ for $n = 0, 1$, and 2. Similar to the previous examples, we can see that the map of $\mathcal{I}(\mathbf{z}, 10; 1)$ yields the most accurate shape of $\Upsilon_1 \cup \Upsilon_2$, but because Υ_1 has a much smaller values of permittivity and permeability than Υ_2 , $\mathcal{I}(\mathbf{z}, 10; n)$ plots Υ_1 much smaller magnitude than Υ_2 .

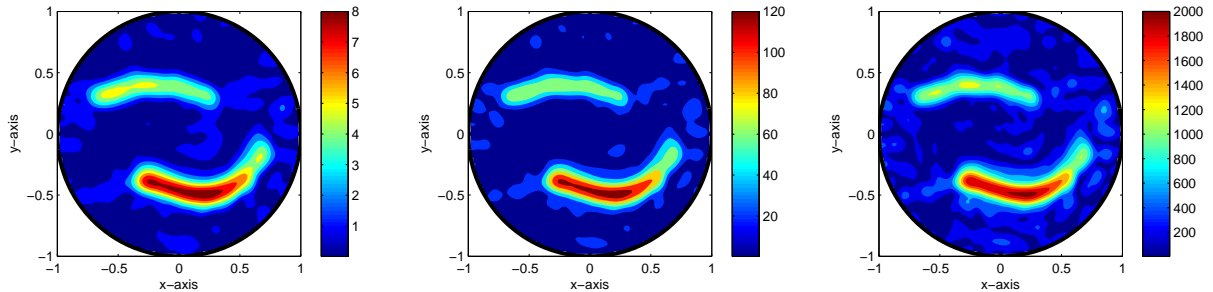


Figure 7: Same as Figure 4 except that the thin inclusions are $\Upsilon_1 \cup \Upsilon_2$.

5. Conclusion and perspectives

We introduced a multi-frequency algorithm weighted by applied frequency for imaging thin electromagnetic inclusions and discussed its properties. The structure of the imaging function and the corresponding numerical experiments show that the proposed imaging algorithm is effective and robust against a large amount of random noise; however application of a large number n in (8) does not guarantee a good imaging result.

We considered a full-view inverse scattering problem, but based on our contributions [15, 18], the proposed algorithm is also applicable to the limited-view inverse problem when the measured boundary data is affected by randomly distributed small inclusions. Therefore, extension of the algorithm to the limited-view inverse problem affected by random scatterers will be an interesting research topic.

References

- [1] M. Abramowitz and I. A. Stegun, Handbook of Mathematical Functions, with Formulas, Graphs, and Mathematical Tables, (1996), Dover, New York.
- [2] D. Álvarez, O. Dorn, N. Irishina, and M. Moscoso, Crack reconstruction using a level-set strategy, *J. Comput. Phys.*, 228 (2009), 5710–5721.
- [3] H. Ammari, An Introduction to Mathematics of Emerging Biomedical Imaging, Mathematics and Applications Series, 62 (2008), Springer-Verlag, Berlin.
- [4] H. Ammari, J. Garnier, H. Kang, W.-K. Park, and K. Sølna, Imaging schemes for perfectly conducting cracks, *SIAM J. Appl. Math.*, 71 (2011), 68–91.
- [5] H. Ammari, H. Kang, H. Lee and W.-K. Park, Asymptotic imaging of perfectly conducting cracks, *SIAM J. Sci. Comput.*, 32 (2010), 894–922.
- [6] E. Beretta and E. Francini, Asymptotic formulas for perturbations of the electromagnetic fields in the presence of thin imperfections, *Contemp. Math.*, 333 (2003), 49–63.
- [7] D. Colton, H. Haddar and P. Monk, The linear sampling method for solving the electromagnetic inverse scattering problem, *SIAM J. Sci. Comput.*, 24 (2002), 719–731.
- [8] O. Dorn and D. Lesselier, Level set methods for inverse scattering, *Inverse Probl.*, 22 (2006), R67–R131.
- [9] I. S. Gradshteyn and I. M. Ryzhik, Table of Integrals, Series, and Products, (2007), Academic Press.
- [10] R. Griesmaier, Multi-frequency orthogonality sampling for inverse obstacle scattering problems, *Inverse Probl.*, 27 (2011), 085005.
- [11] Y. D. Jo, Y. M. Kwon, J. Y. Huh and W.-K. Park, Structure analysis of single- and multi-frequency imaging functions in inverse scattering problems, submitted, available at <http://arxiv.org/abs/1208.0641>.
- [12] A. Kirsch and S. Ritter, A linear sampling method for inverse scattering from an open arc, *Inverse Probl.*, 16 (2000), 89–105.
- [13] Y.-K. Ma, P.-S. Kim and W.-K. Park, Analysis of topological derivative function for a fast electromagnetic imaging of perfectly conducting cracks, *Prog. Electromagn. Res.*, 122 (2012), 311–325.
- [14] W.-K. Park, Non-iterative imaging of thin electromagnetic inclusions from multi-frequency response matrix, *Prog. Electromagn. Res.*, 106 (2010), 225–241.
- [15] W.-K. Park, On the imaging of thin dielectric inclusions buried within a half-space, *Inverse Probl.*, 26 (2010), 074008.
- [16] W.-K. Park, Topological derivative strategy for one-step iteration imaging of arbitrary shaped thin, curve-like electromagnetic inclusions, *J. Comput. Phys.*, 231 (2012), 1426–1439.
- [17] W.-K. Park and D. Lesselier, Electromagnetic MUSIC-type imaging of perfectly conducting, arc-like cracks at single frequency, *J. Comput. Phys.*, 228 (2012), 8093–8111.
- [18] W.-K. Park and D. Lesselier, Fast electromagnetic imaging of thin inclusions in half-space affected by random scatterers, *Waves Random Complex Media*, 22 (2012), 3–23.
- [19] W.-K. Park and D. Lesselier, Multi-frequency imaging of perfectly conducting cracks via boundary measurements, submitted, available at <http://arxiv.org/abs/1207.1812v1>.
- [20] W.-K. Park and D. Lesselier, MUSIC-type imaging of a thin penetrable inclusion from its far-field multi-static response matrix, *Inverse Probl.*, 25 (2009), 075002.
- [21] W.-K. Park and D. Lesselier, Reconstruction of thin electromagnetic inclusions by a level set method, *Inverse Probl.*, 25 (2009), 085010.
- [22] W.-K. Park and T. Park, Multi-frequency based direct location search of small electromagnetic inhomogeneities embedded in two-layered medium, in revision.
- [23] W. Rosenheinrich, Tables of Some Indefinite Integrals of Bessel Functions, available at <http://www.fh-jena.de/~rsh/Forschung/Stoer/besint.pdf>.